Passive appendages improve the maneuverability of fish-like robots

Beau Pollard Phanindra Tallapragada

***Abstract*— It is known that the passive mechanics of fish appendages play a role in the high efficiency of their swimming. A well known example of this is the experimental demonstration that a dead fish could swim upstream [1]. However little is known about the role if any of passive deformations of a fish-like body that could aid in its maneuverability. Part of the difficulty investigating this lies in clearly separating role of actuated body deformations and passive deformations in response to the fluid structure interaction. In this paper we compare the maneuverability of several fish shaped robotic models that possess varying numbers of passive appendages with a fish shaped robot that has no appendages. All the robots are propelled by the oscillations of an internal momentum wheel thereby eliminating any active deformations of the body. Our experiments clearly reveal the significant improvement in maneuverability of robots with passive appendages. In the broader context of swimming robots our experiments show that passive mechanisms could be useful to provide mechanical feedback that can help maneuverability and obstacle avoidance along with propulsive efficiency.**

I. INTRODUCTION

Presently unmanned aquatic vehicles are used to accomplish a multitude of tasks including environmental monitoring, search and rescue, monitoring submerged structures, as well as numerous military applications, and each of these tasks require a different combination of propulsion characteristics. A robot performing environmental monitoring would need to be energy efficient so that it could collect data for long periods of time, while a search and rescue robot would need to be capable of fast speeds. Alternatively, a robot monitoring submerged structures would need to be maneuverable. Traditionally these robots would be propeller driven, but in the past two decades there has been an emergence of research into robots seeking to mimic the locomotion characteristics of natural swimmers [2]–[9].

Flexible bodies can passively deform in response to the forces exerted by the fluid. Experiments and computational studies on the propulsive performance of heaving flexible panels has shown that there is a relationship between parameters such as panel stiffness, panel length, heaving frequency and amplitude, which results in an increase in propulsive performance [10]–[12]. Additionally there has been significant research into the motion of natural swimmers with different fins during their propulsive gaits, using Particle Image Velocimetry (PIV) and numerical simulations [13]–[15], which conclude that the passive deformations of fins could perhaps improve propulsive efficiency. There are other examples that discuss the role of passive deformations of the body or passive structures on the body in swimming by several species [16]–[23]. However, identifying the deformations of fins or the body in the motion of live fish as active or passive can be difficult. In [20] the authors state "Extreme bending of fish fins can be observed during rapid movements [24], and the relative contribution of active and passive deformation remains unclear for the vast majority of cases studied." In a well known experiment, [1], it was demonstrated that the passive deformations of a euthanized trout can provide net forward propulsion when placed down stream from a fixed bluff cylinder. This demonstrated that passive mechanisms in fish can harvest energy from a vortex wake.

The majority of research on passive mechanisms has focused on the resulting improvement of swimming efficiency while their effect on other aspects of motion such as maneuverability are not as well understood. To overcome such difficulties, we investigated the motion of three fish like robots with differing tail morphologies. In all three cases the tails are entirely passive, responding to the fluid-robot body interaction. The robots do not possess any active appendages nor actively deform in shape. All the robots are propelled by the oscillations of an internal momentum wheel, [25], thereby eliminating any active deformations of the body. We also compare the motion of robots with passive tails to the motion of a robot without any tail like appendages. Our experiments clearly reveal the significant improvement in maneuverability of robots with passive appendages.

In the context of robots, the benefits from passive mechanisms could include mechanical feedback simplifying computational costs of control, which is the case in motion of many animals, [26]. For instance insect's muscle-tendon system and flexible joints in their legs allow them to quickly adapt to small inconsistent bumps along their trajectory without having to actively compensate [27]. The running hexapod described in [27] encompassed the passive flex in the muscles and joints through the use of pneumatic linear actuators. The compressed air in the actuators acts similar to a spring and allows the robot to achieve a high rate of speed over rough terrain. In the case of swimming robots, such mechanical feedback gained through passive mechanisms could prove useful in such tasks as obstacle avoidance and greatly improve the agility of robots.

The paper is structured as follows. In section II we present the different robot models that will be tested and compared. Three of the models utilize the same main body with different tail configurations while the one solid body model is used as a benchmark to which the others will be compared. In section III, the testing apparatus is described as well as the

Beau Pollard and Phanindra Tallapragada are with the Department of Mechanical Engineering, Clemson University, Clemson, SC 29634, USA.
Correspondence should be directed to `ptallap@clemson.edu`.

This is the author's version of an article that has been published in this journal. Changes were made to this version by the publisher prior to publication.
The final version of record is available at http://dx.doi.org/10.1109/TMECH.2019.2916779

inputs to the robots for each subsequent test. In section IV, the results from the tests are presented and compared to each other as well as with other robots presented in literature. In section V computational results in support of the experiments are presented.

II. PHYSICAL MODELS

In the experiments four different robots were tested which utilized two different main bodies and three different tail combinations. The robots tested are shown in Fig. 1. The robot in Fig. 1 (a) is a solid body hydrofoil, (b)-(d) have main bodies with similar dimensions as (a), but they poses passive tails. The passive tails are not actuated and are not connected with springs so only the fluid-body interaction causes the tails to rotate. Throughout this paper the robot in Fig. 1 (a)-(d) will be denoted as robots A, B, C, D respectively.

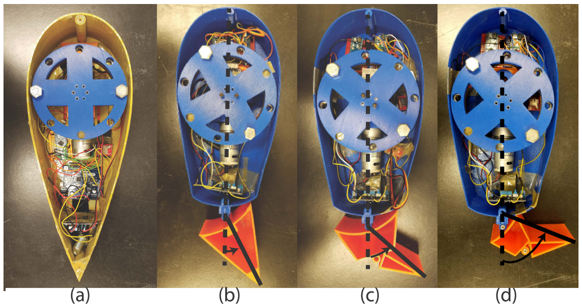
(a) (b) (c) (d)

Fig. 1. Four different robots. Models B, C, D have tails. The degree of rotation of the tail assembly is the angle made by the solid black line with the dotted line.

The main bodies of the robots are modeled to have the horizontal cross section of a NACA 0030 airfoil, with a length of 36.5 cm, it is 14 cm at its widest point and has no camber. All of the robots were designed to have similar characteristics. The total lengths of the fabricated robots are between 36.5 cm and 37.5 cm, with weights in the range of $1.15 - 1.19$ kg (see Table I) and possess the same internal components such as batteries, micro controllers, motors and internal rotors. The main bodies of all the models are geometrically the same, and they house the motor, internal momentum wheel, micro controllers, and batteries. The modular design allows us to easily change the morphology of the tail segments.

A 2-D representation of the four robots is shown in Fig. 2. In Fig. 2 X_b represents the body fixed longitudinal axis, which is formed by drawing a line connecting the front tip of the robot to the center of the internal rotor, and Y_b is the body fixed axis orthogonal to X_b. The inertial axis X is parallel to the longitudinal axis of the pool and the Y axis is parallel to the lateral axis of the pool. The angle θ represents the difference in angle between the X_b axis and the inertial X axis.

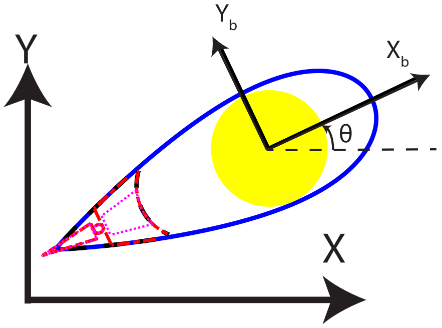

Fig. 2. Coordinate definitions of the robots

In Fig. 2 the blue line represents the body of robot A. The blue line up until the different colored dashed lines represents the main bodies of all four of the robots. Robot B's tail, which is 10 cm long is represented by the black dashed line. Robot C's tail is represented by the red dashed line. It is made up of two separate segments, the first segment, attached to the main body, measuring 4.5 cm in length and the second segment is an isosceles triangle measuring 6 cm in length and 2 cm at the base. Robot D's tail is made up of two separate segments and is represented by the magenta dashed lines. The first tail segment is in the shape of a trapezoid with a base width of 4.5 cm, a top width of 2.5 cm and a length of 4.5 cm. The second tail segment of robot D is the same as the second tail segment of robot C. Since robots B, C and D have different tail configurations they also have different possible degrees of rotation. We define the degree of rotation of the tail assembly to be the highest possible angle made by the X_b axis of the robot with a line that connects the trailing edge of the tail assembly to the point at which the tail assembly is connected to the main body. The degree of rotation of tails for robots B, C and D are 27^o, 50^o and 80^o respectively.

The means of propulsion of these robots is unique because the only actuation is through the oscillations of an internal momentum wheel. We briefly describe the dynamics of hydrofoils with internal momentum wheels and refer the reader to earlier work, [28]–[31] for details. The locomotion of the robots depend on the change in inertia tensor, and the shedding of vortices past their tailing edge, which is similar to the way many natural swimmers propel themselves. The rotation of the internal momentum wheel causes the main body of a robot to rotate in the opposite direction due to the conservation of angular momentum. In the case of robot A the rotation of the body causes the rolling up of vorticity at the trailing edge. The shedding vortices impart momentum to the body and propel it forward. In the case of robots B, C, and D the rotation of the main body can cause the tail(s) to rotate and do so possibly at a different angular velocity. Vorticity is once again shed at the trailing edge of the tails providing the necessary propulsive force. In the robots with tails an additional propulsive factor exists; the oscillations of the tail cause the body inertia tensor and the added mass tensor to change periodically. The interaction of a body with periodically varying inertia and vortex shedding causes additional propulsion. More importantly from the perspective of maneuverability, in the robots possessing tails, the coupled fluid-body dynamics passively re-orient the tails, which changes the location where the vortices are shed relative to the main body. This passive change of the location of vorticity causes a change in the moment exerted on the body.

The momentum wheel inside the robots is displayed in Fig. 1 as the blue colored wheel and the yellow colored circle in the representative diagram in Fig. 2. The balanced rotor is a steel ring of outer diameter 13.2 cm and an inner diameter of 10.2 cm with a thickness of 0.95 cm. The moment of inertia of the rotor about an axis passing through its center is 14.661 kg·cm^2. The rotor is driven by a IG32 right angle 12V DC motor which is bolted to the bottom of the robot's body. The motor is controlled using an SainSmart L298H motor driver and an Arduino Micro. A SparkFun Triple Axis Accelerometer and Gyro Breakout-MPU-6050 is positioned directly in front of the motor, in the approximate center of gravity of the robot, to measure the angular velocity of the robot. The gyro data received by the accelerometer is saved onto a SanDisk ultra 32GB microSD card, using a SparkFun microSD shield connected to an Arduino Micro. The Arduino Micro is also used to control the accelerometer. The robot is powered by a LiPo 1000mAh 7.4V battery pack.

III. EXPERIMENTS

The experiments conducted were designed to determine the maneuverability of the different robots. We define maneuverability of a robot as its ability to execute a change in its heading angle, $\Delta\theta$. A common benchmark for the change in this heading angle is for the robot to execute a 180^o turn. There are two possible measures for maneuverability, the time (t_r) it takes a robot to turn 180^o and the displacement of the robot's centroid in the while executing this turn. A shorter turning time shows an ability to execute fast turns and a smaller turning displacement shows the ability to execute turns in an environment with close obstacles.

In the experiments two different types of inputs were applied via the internal momentum wheel. To get the robots to acquire a translational speed moving along a straight line, the momentum wheel would execute sinusoidal motion, $\omega(t) = A\sin\nu t$. During such periodic oscillations of the internal momentum wheel the robots center of mass moves along a serpentine path, with average motion being a straight line, [25]. To turn a robot quickly, the momentum wheel would spin with a constant angular velocity, ω_r in one direction, forcing the robot to counter rotate. We adopt this approach as this allows the possibility of fast turns. Throughout all of the tests when a robot is executing a turn, the momentum wheel is prescribed to spin at a constant rate of $\omega_r = 825[^o/s]$, which is the maximum speed of the DC motor used in the robots. The speed of the rotors during the experiments was measured by using the camera to track the angular displacement of the two bolts attaching the rotor to the motor (see Fig. 1). The angular velocities of the rotor, measured from the images, were always within the range of $[770°/s - 830°/s]$, i.e., an error of less than 7% could be present in the angular velocity of the rotor.

The tests were conducted in a pool that was 2.4 m long and 1.2 m wide. Gyro data was collected using an LSM9DSO accelerometer/gyroscope mounted at the approximate center of mass of the robots and the position of the robot was tracked using a camera mounted 2.15 m above the pool. The camera records data at the rate of 30 frames per second. In our experiments, this rate is sufficient to identify changes in the orientation angle of the robots that are as small as 3 degrees between each frame. For all of the tests the gyro data was integrated using the trapezoidal rule to get the angular orientation of the center of mass of the robot. The angular displacement thus obtained was verified with the acquired images of the robot at frequent intervals of time.

IV. RESULTS

A. Turning from rest

At the start of the experiment the robots were placed in the pool with their body axes X_b parallel to the wall of the pool. The internal momentum wheels had a constant angular velocity of $\omega_r(t)$ for 15 seconds. Their angular orientation $\Delta\theta$ throughout the tests are shown in Fig. 3. This test measures the ability of a robot to execute a turn beginning from rest.

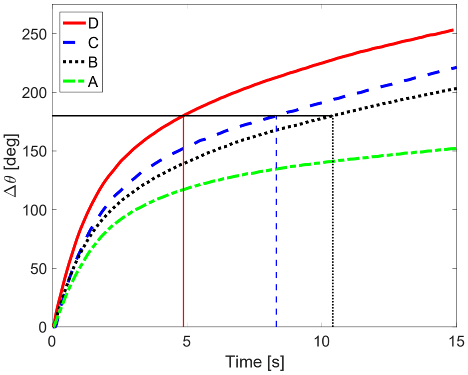

Fig. 3. Change in heading angle of the robots when they begin executing a turn at rest.

From Fig. 3 it's apparent that robot D demonstrated the best turning performance, with $\Delta\theta \approx 250^o$ and with the turning time for a 180^o turn being $t_r \approx 4.9$ seconds. Robot C achieved a total angular displacement of $\Delta\theta \approx 235^o$ and had a turning time $t_r \approx 8.3$ seconds for a 180^o turn. Robot B robot turned a total of $\Delta\theta \approx 225^o$ and had a turning time $t_r \approx 10.4$ seconds for a 180^o turn, and robot A was only capable of achieving a total angular displacement of $\Delta\theta \approx 155^o$.

The results of this test show that the addition of passive tail segments in robot D increases the total turning angle $\Delta\theta$ of the robot by 61% when compared to the turning angle of robot A. More significantly the robots with passive tails can execute a full 180^o turn while robot A cannot. We do see that robot D's turning time decreased by 41% and 53% when compared to robots C and B respectively. The decrease in turning time of robot D over robots C and B and of robot

C over robot B can be attributed to the increasing degree of rotation of the tails for robots C and D.

B. Turning after achieving a set velocity

It is possible that the maneuverability of a robot could change significantly depending the speed with which the robot is moving. To check if the passive tails can improve maneuverability in such cases, we performed experiments wherein the robots begin the turning motion at a non zero speed. The momentum wheels of the robots first executed sinusoidal oscillations, $\omega(t) = A \sin \nu t$ until the robots acquired an average translational velocity of 10 cm/s. Once this velocity was reached a constant angular velocity $\omega(t) = \omega_r$ was applied to the internal momentum wheel.

The graphs of the heading angles of the main body of the robots are shown in Fig. 4. Robot D reached a total angular displacement of $\Delta\theta \approx 295^o$ and achieved a displacement of 180^o in $\approx$ 4.1 seconds. Robot C accomplished an angular displacement of $\Delta\theta \approx 224^o$ and reached a displacement of 180^o in $\approx$ 7.38 seconds. Robot B reached a total angular displacement of $\Delta\theta \approx 204^o$ and reached 180^o in $\approx$ 11.79 seconds, and robot A could only reach a total angular displacement of $\Delta\theta \approx 110^o$. Since the robots turns were started after achieving a predefined speed, there was some lateral translation during the turning phases. Fig. 5 shows the overlaid images of the robots at different times during these maneuvers to demonstrate the variation in turning displacement. From the images in Fig. 5 the turning displacement is measured as the lateral displacement the robot traveled before completing a $\Delta\theta = 180^o$. Robot D has a turning displacement of approximately 20 cm, which corresponds to approximately 0.53 BL body lengths (BL). Robot C has a turning displacement of approximately 27 cm or 0.72 BL. Robot B has a turning displacement of approximately 35 cm or 0.97 BL. Robot A was not capable of turning 180^o.

The turning dynamics of the robots when they execute a turn starting from rest versus when they begin executing the turn when moving at a speed of 10 cm/s are compared in Fig. 6. The sub figures (a) to (d) in Fig. 6 show the data for the turning motion for robots A to D respectively. While the total angular displacement that the robots could achieve in 15 seconds while moving at a speed of 10 cm/s increased for robot D the change for robots C and B was negligible with a small decrease. In the case of robot A the angular displacement that could be achieved when moving at 10 cm/s decreased significantly by about 45^o. Alternatively the turning time for robot D decreased by about 0.8 s or 16% when it is moving at 10 cm/s compared to when it executes a turn beginning from rest. The turning time for robot C decreased by about 0.9 s or 10%. The turning time for robot B increased by 1.4 s or 13.5%.

A clear pattern emerges regarding the effect of speed on robots with tail like segments and the maneuverability of the robots. Both of the robots possessing two tail segments turned 180^o faster when the turn was started from a non zero velocity and robot D turned $\approx 18^o$ farther when the turn was started from a set velocity. Robot B with a tail that offered only a limited degree of rotation performed marginally worse when its turn started from a set velocity. Robot A's maneuverability was significantly worse when its turn started from a set velocity. The general trend is that robots whose tails have a large degree of rotation demonstrate improved maneuverability relative to those of robots without tails or with limited degree of rotation tails. Moreover this maneuverability of robots with tails seems to improve even more when the robots are moving with a small velocity while the maneuverability decreases for robots without a tail.

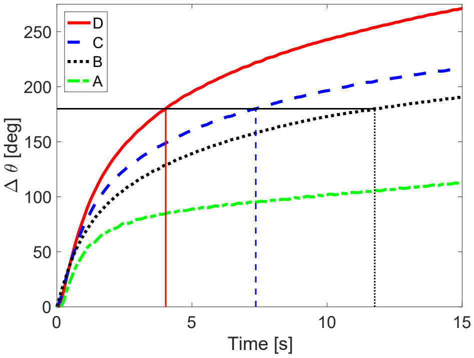

Fig. 4. Change in heading angle of the robots when they begin executing a turn moving at a constant speed of 10 cm/s.

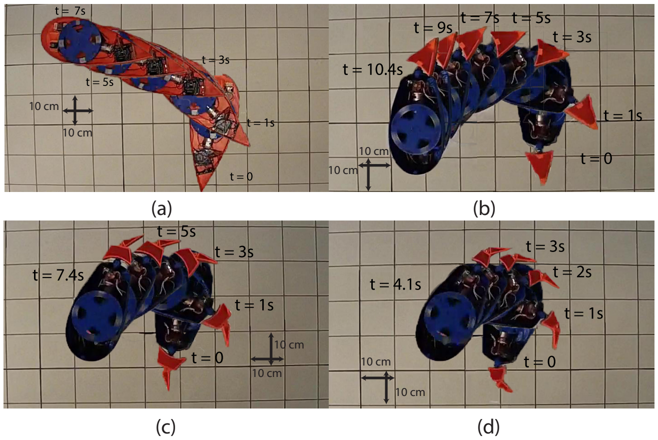

(a) (b)

(c) (d)

Fig. 5. Overlaid images of the robots performing turns with a constant ω_r (a) Robot A, (b) Robot B, (c) Robot C, (d) Robot D

In both the turning tests all four robots initially rotated quickly at the beginning of their turns before their rotation stalls, as observed by the high initial slope of the graphs in figs. 3 and 4 and subsequent decrease in slope. The decrease in the rate of rotation falls off more slowly as the tail segments of the robot offer more degree of rotation. In Fig. 5 it can be observed that once turning motion begins, the tail segments of robots B, C, and D rotate in an opposite direction to the main body. In fact this is a generic feature of motion of the robots with passive tail segments. We performed experiments where the rotor executes sinusoidal oscillations to generate average straight line motion for the robot. Periodic motion of the rotor results in oscillations of the main body

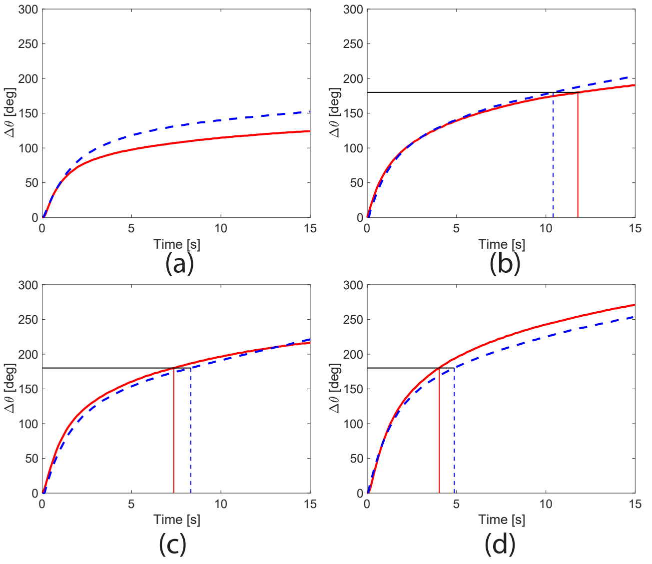

Fig. 6. Comparison of the turning motion of robots between the cases when they begin from rest (blue dotted line) and when they begin the turn at a speed of 10 cm/s (solid red line).

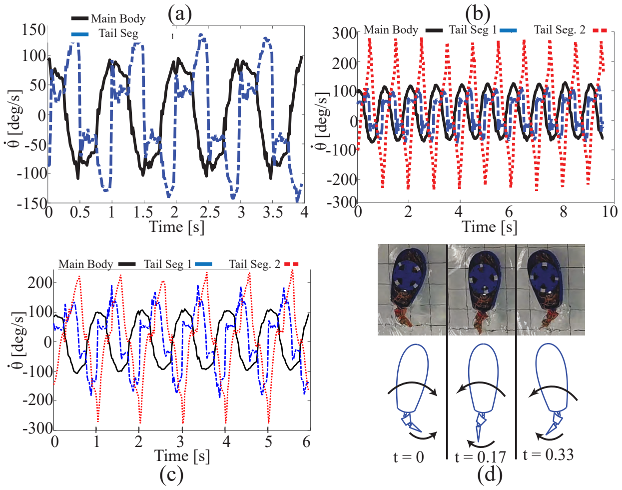

Fig. 7. Angular velocities of the tail segments and main body of (a) Robot B with a single tail, (b) Robot C with two tails and (c) Robot D with two tails. (d) Snapshots of Robot D during average straight line motion showing relative angular motion of the tail segments and the main body.

and allows the observation and consistent evaluation of the relative motion of the tail like segments. Fig. 7(a)-(c) show the angular velocities of the main bodies of robots B, C and D, respectively, and their tail segments, recorded by gyroscopes during such periodic forcing of the momentum wheel. The measured angular velocity of the tails for robots B, C and D have a phase difference ranging between 170° and 180° in different runs of the experiments with respect to the angular velocity of the main body. This phase difference implies that the angular velocity of the tails is in an opposite direction to the main body, as illustrated by the snapshots in Fig. 7(d) spanning an interval of 0.33s. However once the tails reach their maximum possible deflection, they move in the same direction as the main body.

V. TAILS MODIFY THE HYDRODYNAMIC MOMENT

A qualitative explanation for the influence of the tail in the turning motion of a robot can be found in the differing directions of the angular velocities of the main body and the tail, such as shown in Fig. 7. These differences change the fluid-robot interaction via vortex shedding at the trailing edge of the robots. The fluid-body interaction can be modeled within the framework of inviscid fluid dynamics. The Reynolds number, which is the ratio of the inertial to the viscous forces defined as $Re = \frac{VD}{\nu}$ for a body of length D moving with a velocity V in a fluid with viscosity ν, associated with the motion of the robot is of the order 10^4. In this regime of fluid flow, the viscous effects are significant only in a thin region around the body, with the fluid away from the body behaving as an inviscid one, [32]. The viscous effects that are important in a small region around the body lead to vorticity peeling off from the body; this phenomenon is modeled using the Kutta condition in the inviscid framework, [33], [34]. The steady Kutta condition requires that vorticity be created at the trailing edge of the body and that its strength and sign (clockwise vs counterclockwise) is such that the relative velocity of the fluid with respect to the velocity of the trailing edge is zero.

When a body like that of robot A is spinning about its center with an angular velocity of Ω, the velocity of the trailing edge of the body is $v_t = \Omega \times L_t$ where L_t is the position vector of the trailing edge relative to the center of the body. The vorticity that is created at the trailing edge is such that the fluid velocity at this trailing edge is in the same direction as v_t. As Fig. 8(a) shows the circulation of the vortex that is created has a direction opposite to the angular velocity of the body. The resulting hydrodynamic moment because of this vorticity opposes the turning motion of the robot.

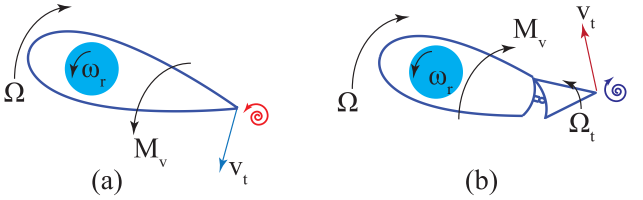

Fig. 8. Interaction of a spinning robot with vorticity that is created at the sharp trailing edge, (a) Robot A, (b) Robot B.

When a body like that of robots B, C or D is spinning about its center with an angular velocity of Ω, the tail assembly spins with an angular velocity Ω_t that is in a direction opposite to Ω. The velocity of the trailing edge of the tail v_t is now in the opposite direction compared to the case of robot A. The vorticity that is created at the trailing edge of the passive tail has a circulation that is in the same direction as the angular velocity of the main body. The resulting hydrodynamic moment that is exerted on the body aids in the rotation of the body.

A. Computation of hydrodynamic moment

The hydrodynamic moment experienced by a rapidly turning robot with tails that deflect by large angles can be challenging to compute directly due to the unsteady fluid-body interaction that occurs over a fast time scale. However quantitative insight into the experiments can be obtained by computing the moment experienced by the foil-like body in its average straight line motion during one time period of its oscillation. The computations described in this section show that the phase difference between the tail motion and that of the main body, described in Fig. 7 leads to a significant difference in the hydrodynamic moment on the body. The computations are based on the well known two dimensional panel method [35]–[37], and only a brief description is given here. In this method the body is discretized into straight lines (panels), the fluid motion is modeled using the unsteady Bernoulli equation, the viscous effects leading to vortex shedding are modeled by the unsteady Kutta condition and an average fluid drag coefficient models the frictional resistance to motion in the fluid.

Taking this approach, simulations were performed on a two dimensional body shown in Fig. 9. The foil geometry is that of a NACA 0030 airfoil with the last quarter being a movable tail, similar in geometry to robot B. The fluid dynamic equations were nondimensionalized by the chord length of the foil and the density of the fluid. In general a 2D panel method breaks a body up into N straight line segments. The boundary conditions we enforce are that the fluid velocity relative to the normal direction of the panel at the panels midpoint is zero. The boundary conditions are satisfied by placing N sources (σ), which vary in strength from panel to panel and a vortex distribution (γ_b) which remains constant from panel to panel. The i^{th} panel is highlighted in Fig. 9, there the CW vortex strength γ_b and the source strength σ_i are represented by the blue and black arrows respectively. The fluid motion is modeled using the unsteady Bernoulli equation,

$$p + \frac{1}{2}||\mathbf{u}||^2 + \frac{\partial \phi}{\partial t} = constant \tag{1}$$

where $\frac{\partial \phi}{\partial t}$ is the partial derivative of the fluid velocity potential function with respect to time, p is the pressure and $||\mathbf{u}||$ is the fluid velocity. The fluid velocity potential is a function of the current sources and vortex strengths as well as the previously shed vorticies. The source and vortex strengths are the $N+1$ unknowns that need to be solved for using the applied boundary condition at each control point and an additional constraint, which is the Kutta condition. In particular, applying the Bernoulli equation to the first $(i = 1)$ and the last panels, $(i = N)$ that enclose the sharp trailing edge,

$$p_1 + \frac{1}{2}||\mathbf{u}_1||^2 + \frac{\partial \phi_1}{\partial t} = p_N + \frac{1}{2}||\mathbf{u}_N||^2 + \frac{\partial \phi_N}{\partial t}. \tag{2}$$

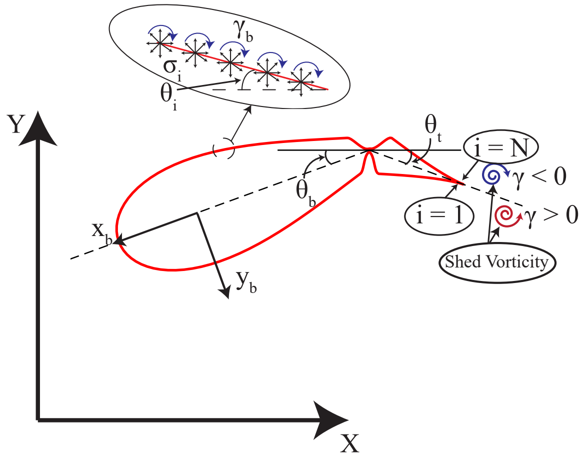

Fig. 9. Schematic of the foil used in the panel method simulations. Each panel has a source distribution σ and a vortex distribution γ_b

The Kutta condition acts as a way to impose viscous effects in a small region of a body submerged in a potential fluid. As the trailing edge panels lengths converge to zero in finer panel discretizations, the trailing edge becomes a stagnation point. Therefore the pressures on the two panels at the trailing edge are set equal to one another, $p_1 = p_N$. If two points x_1 and x_2 are connected by a path s then the change in potential between the two points is given by $\Delta\phi = \int_{x_1}^{x_2} \mathbf{u} \cdot ds$, where $\mathbf{u}$ is the fluid velocity along the path s. Evaluating the integral along the surface of the foil in the clockwise direction is defined as being equal to the circulation enclosed by the path:

$$\Delta\phi = \int_1^N \mathbf{u} \cdot ds = \Gamma_b. \tag{3}$$

Around the sharp trailing edge, setting $p_1 = p_N$ in (2) and using (3) the Kutta condition can be written in terms of the rate of change in circulation

$$||\mathbf{u}_1||^2 - ||\mathbf{u}_N||^2 = 2\frac{\partial \Gamma_b}{\partial t} \tag{4}$$

where Γ_b is equal to $\frac{L\gamma_b}{2\pi}$ where L is the perimeter of the foil.

Once the source and circulation strengths around the body are determined, (1) is applied to each panel resulting in the computation of the pressure, p_i, on the i^{th} panel. Multiplying p_i by the length of the i^{th} panel results in the hydrodynamic force $\mathbf{F}^i$ on the i^{th} panel. The hydrodynamic moment, $\mathbf{M}_h$, experienced by the body is then

$$\mathbf{M}_h = \sum_{i=1}^{N} \mathbf{r}_i \times \mathbf{F}^i \tag{5}$$

where $\mathbf{r}_i$ is the position vector of the center of the i^{th} panel with respect to the center of mass of the body. After forces and moments are calculated the point vortex at the trailing edge is released into the fluid and the simulation takes one time step forward.

In the simulations the foil was fixed at the origin in a free-stream velocity. This simulates the motion of a body in quiescent fluid with a reference frame attached to the body.

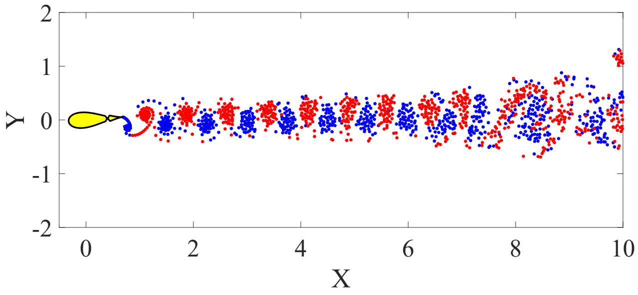

Fig. 10. Simulation of a foil fixed at the origin with prescribed periodic oscillations for the main body and the tail. Red and blue dots represent positive and negative circulation point vorticies respectively.

The free stream velocity was chosen to be half a body length per second. Sinusoidal angular velocities were prescribed to the main body and the tail segment. The angular velocities were assigned such that they mimic the angular velocities measured in the experiments, Fig. 7. Throughout all of the simulations the main body oscillated at an amplitude of 15°. The frequency of oscillations was held constant at 2π, which is the same as the forcing frequency applied to provide straight line motion in the experiments. A range of values of the phase lag between the main body and tail and two values of amplitudes of tail oscillations were investigated. The values of tail amplitude, A_t relative to the main body in the simulation were 30° and 45°. The values of A_t are measured in the same way that the degree of rotation was measured in the experimental test beds and the values were chosen because they are similar to the maximum tail displacements of robots B (27^o) and C (50^o). The phase lag (ϕ_t) imposed on the tail for each value of A_t ranged from $\phi_t = 0°$ to $\phi_t = 180°$ increasing by an interval of $10°$. A snapshot of the vortex wake formed for steady swimming is shown in Fig. 10 where each red dot represents a counter clockwise (CCW) vortex and each blue dot represents a clockwise (CW) vortex.

Hydrodynamic moment can either assist or resist the turning motion of the swimmer. An assisting hydrodynamic moment occurs when the sign of the moment acting on the body from the fluid is in the same direction as the rotational velocity of the body. Additionally, the sign of the vorticity that is most recently shed can be used as a proxy to identify whether the hydrodynamic moment is assisting or resisting the rotation of the main body. The influence of a vortex sheet varies as the inverse of the square of the distance from the vortex to the point of interest. So the closer a vortex is to the point of interest the larger the affect will be, which means the most recently shed vorticity will have the largest influence on the body. If the recently shed vorticity is rotating in the same direction as the body, it will exert a moment on the body that is in the same direction as the rotation of the body. Alternatively, vorticity rotating opposite to the body's rotation will hinder the turning motion of the body. Our simulations show that the motion of a tail with a phase lag relative to the main body can change the sign of the shed vorticity, as shown in Fig. 11.

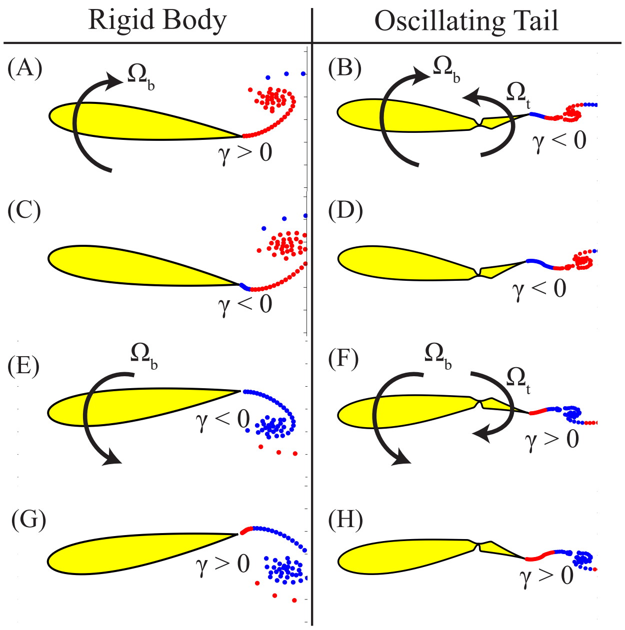

Fig. 11. Rigid foil and foil with a tail oscillating with a phase lag of 180° and previously shed point vorticies. Ω_b in (A) and (B) was -60 $[°/s]$, Ω_b in (C), (D), (G) and (H) was 0 $[°/s]$ and Ω_b in (E) and (F) was 60 $[°/s]$. Ω_t in (B), (D), (F), and (H) was -120 $[°/s]$, 0 $[°/s]$, 120 $[°/s]$, and 0 $[°/s]$

The left side of Fig. 11 shows four snapshots of the rigid foil at different points of one periodic oscillation and the right side of Fig. 11 is the foil with a tail oscillating with an amplitude of 45° and a phase lag of 180° at the same points of one periodic oscillation. In both of the cases the main body rotated with an amplitude of 15° and a frequency of 2π. The red and blue dots are point vorticies shed from the trailing edge with strength γ and Ω_b is the angular velocity of the main body. The black arrows overlaid on the main bodies show the direction of the angular velocity of the main body. The black arrows overlaid on the tail segments in Fig. 11 (B) and (F) show the direction of the tail segments angular velocity. In Fig. 11 (C) the rigid body is shedding a vortex with $\gamma > 0$, which is opposite of the direction of the main body, i.e., the vortex induced hydrodynamic moment is resisting the rotation. The oscillating tailed robot, Fig. 11 (D), is shedding vorticity with $\gamma < 0$, which is in the same direction of the main body rotation, i.e. the turning motion is assisted by the vortex induced moment on the body. The same result is presented in Fig. 11 (G) and (H). However once the tails have reached their extreme displacement, relative motion between the tail and the body has ceased, the shed vortices from the trailing edge have the same sign, as shown in Fig. 11 (C), (D) and (G), (H). So there is only a certain fraction of time during each oscillation period where the sign of shed vorticity between a rigid body and a tailed body are different. Figures 12 and 13 show the time dependence of the hydrodynamic moment and shed vorticity for the rigid foil and a foil with a tail for two periods of oscillation of the main body.

A moment that assists a turn (in the same direction as the rotational direction of the robot) will be denoted as $\mathbf{M}^+$ and

$$\begin{aligned} &\mathbf{M}^+ = \mathbf{M}_h \quad \text{if} \quad \Omega_b \cdot \mathbf{M}_h \geq 0 \\ &\mathbf{M}^+ = 0 \quad \text{otherwise}. \end{aligned} \tag{6}$$

The hydrodynamic angular impulse imparted to the robot during a time period $[0, T]$ is $\mathbf{I}_h = \int_0^T \mathbf{M}_h dt$ and the hydrodynamic angular impulse that assists the turn is $\mathbf{I}^+ = \int_0^T \mathbf{M}^+ dt$. In Fig. 12 (A) and Fig. 13 (A) the area under the moment curve is shaded blue when the moment is assisting the turning motion and yellow when it is resisting the turning motion of the foil. The moment on the body with a tail is initially assistive but turns resistive roughly when the tail has reaches its extreme position relative to the main body. The ratio AP_m of the hydrodynamic impulse that assists the turning motion to the total impulse is

$$AP_m = \frac{\mathbf{I}^+}{\mathbf{I}_h}. \tag{7}$$

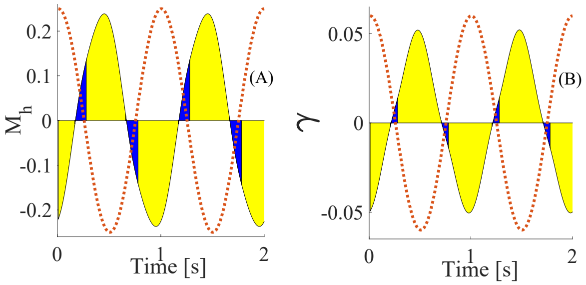

Fig. 12. Hydrodynamic moment (A) and vortex strength (B) for 2 time periods of the rigid body. The yellow region represents the area of resistance and the blue represents the area of assistance. The red dashed line represents a scaled Ω_b to highlight the phase difference with respect to the M_h and γ.

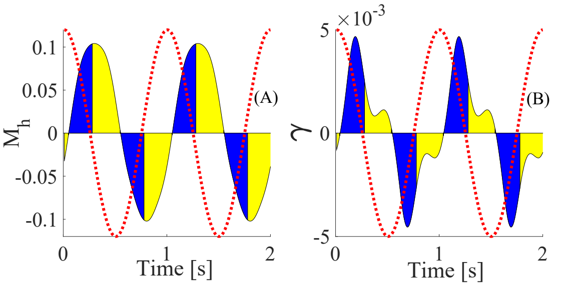

Fig. 13. Hydrodynamic moment (A) and vortex strength (B) for 2 time periods of the foil with the tail 180° out of phase and an oscillation amplitude of 45°. The yellow region represents the area of resistance and the blue represents the area of assistance. The red dashed line represents a scaled Ω_b to highlight the phase difference with respect to the M_h and γ.

For a rigid foil, the hydrodynamic moment is mostly resisting the turning motion of the body, with $AP_m \approx 0.03$ while for a foil with a tail, $AP_m \approx 0.46$. The hydrodynamic moment in fact assists the turning motion of the foil with a tail for almost half the time period of the motion and the assistive hydrodynamic impulse imparted to the body in the initial motion of the tail almost cancels out the subsequent angular impulse that resists the turning. Additionally, the maximum values of the hydrodynamic moment on the foil with a tail were less than half of those on the rigid foil. Therefore an external torque applied to the foil with a tail can be expected to impart a higher angular acceleration. A high level heuristic explanation at the beginning of this section (see Fig. 8) relied on the sign of the most recently shed vorticity relative the angular velocity of the main body. The validity of the sign of the most recently shed wake as a proxy or a surrogate measure for the hydrodynamic moment can be seen in Fig. 12 (B) and Fig. 13 (B), where the area under the graph when the signed function $S_v = sign(\Omega_b \gamma) = 1$ is shown in blue and yellow otherwise. The function S_v changes sign at almost the same time as the hydrodynamic moment changes from assistive to resistive, with the time lag due to the fact that the hydrodynamic moment is influenced not just by the most recently shed vorticity, but by all of the vortex wake.

The phase lag between the oscillation of the tail and the main body is a significant factor that determines the sign of the velocity of the trailing edge (see Fig. 2) and shed vortex wake and the resulting moment on the body. To verify this computations were performed where the phase difference between the angular velocity of the tail Ω_t and the main body Ω_b was varied for two values of the amplitude of tail deflection. In Fig. 14 the x-axis is the phase lag between the main body and the tail, the y axis of Fig. 14 is the AP_m. The red solid line, and blue dashed line represent the A_t values 45°, and 30°, respectively. Increasing A_t increases the AP_m for ϕ_t values greater than 50°. Thus the turning performance is dependent on the range of motion of the tail as well as the phase difference between the tail and the main body. The experiments bear out this result qualitatively, with Robot C turning faster than robot B. The peak values of AP_m for both cases was measured at a phase difference of 160°, and not 180° due to the influence of the near wake.

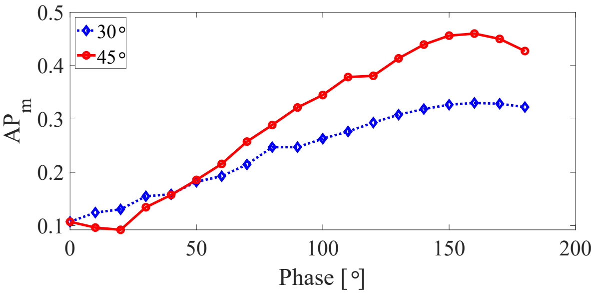

Fig. 14. Portion of the forcing period where the hydrodynamic moment was advantageous to turning. The red, and blue dashed lines are the results from the simulations when A_t was 45°, and 30° respectively. The circles and diamonds represent the data points from the 45° and 30° simulations respectively.

This is the author's version of an article that has been published in this journal. Changes were made to this version by the publisher prior to publication.
The final version of record is available at http://dx.doi.org/10.1109/TMECH.2019.2916779

VI. ALTERNATING BETWEEN PERIODIC AND CONSTANT ANGULAR VELOCITY INPUTS - EXPERIMENTS

Since the robots' rotation stalls because of the vorticity that is created at the trailing edge, a possible way to overcome this stall is for the robots to adopt a strategy of alternating forced rapid spinning and passive dynamics. The momentum wheel rests between bursts of continuous rotation. When the momentum wheel rests, the robots move passively under the hydrodynamic influence. Experiments were performed to check the viability of this strategy. The tests began with the robots swimming on average in a straight line until they reached an average translational speed of 10 cm/s, then a constant angular velocity was applied to the internal momentum wheel for three and a half seconds. This period of 3.5 s was chosen based on the time it takes for the robot's rotation to stall as shown in Fig. 4. The rotor then slowed to a stop before beginning to rotate again with a constant angular velocity. This process was repeated three times and then the momentum wheel resumed periodic oscillations to produce average straight line motion. The input $\omega(t)$ for the test is shown in the top left corner of Fig. 15.

The angular displacement of the robots during this experiment are shown in Fig. 15. It should be noted that the speeds of the robots were all the same when the first constant angular velocity was applied to the internal momentum wheel. Figure 16 shows the x and y position of the center of the robots. Robot D again displays the best maneuverability characteristics. Robot D achieved a total angular displacement of $\Delta\theta \approx 350^o$ and reached 180^o in $\approx$ 5.6 seconds. Robot C turned a total of $\Delta\theta \approx 290^o$ and reached 180^o in $\approx$ 6.3 seconds. Robot B reached a total angular displacement of $\Delta\theta \approx 245^o$ and reached 180^o in $\approx$ 7.5 seconds. Robot A with no tail accomplished a total angular displacement of $\Delta\theta \approx 110^o$. All of the robots achieved larger total angular displacements in shorter times than in the previous tests. The experiments suggest that alternating short bursts of rest-propulsion input could form the basis of an open loop control technique for executing turns.

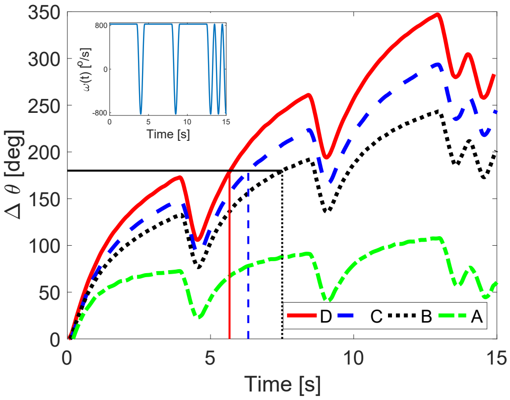

Fig. 15. Gyro data from robots when the input to their internal momentum wheel alternates between constant and periodic angular velocity

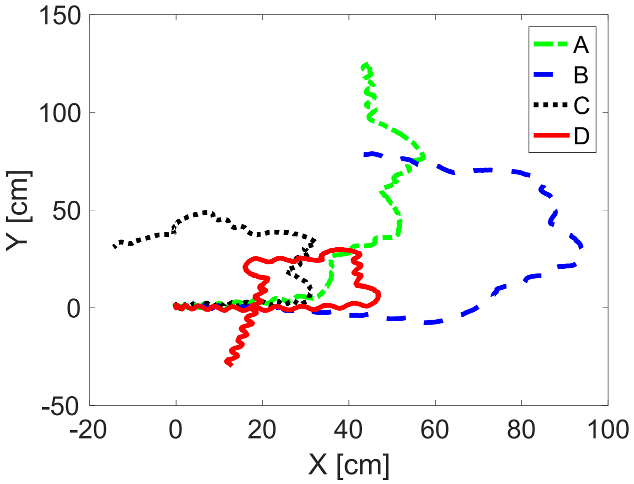

Fig. 16. Path of the robots when momentum wheel alternates between constant spin and rest.

In order to determine the turning radii of the robots during this test, the center of the main bodies of the robots were tracked in consecutive frames of images in recorded movies. A program written in Matlab tracked the main rotor throughout the videos. During this test once the rotor stopped it turned the robot in the opposite direction of the turn, which caused some net forward translation, seen in the wiggling section of the trajectories in Fig. 16.

The turning motion of the robots described thus far is achieved without feedback control. The only actuation is the motion of the internal momentum wheel. A significant ability to turn is achieved through the passive tail segments. This ability to turn is comparable to or even better than that of many robots with multiple actuators and sensors and using feedback control algorithms. To show this we compare the maneuverability of the robots with passive appendages presented in this paper with those of other aquatic robots whose data have been published. We have mostly selected data on aquatic robots whose body length is nearly the same as that of the robots discussed in this paper. The results are summarized in table I.

The most maneuverable robots are those presented in [40]- [42]. The robot discussed in [40] has two actuated tail segments which are controlled by two servomotors, the dolphin like robot discussed in [41] has a total of five control inputs with four servomotors controlling joints in the tail and one controlling an internal moving mass. The robot in [42] has four servomotors controlling four joints in the tail. The robots in [40]- [42] have many control inputs and do not utilize the passive dynamics inherent in the robot-fluid interaction. Robot D that is presented in this paper has only one control input but two passive joints in the tail assembly and utilizes no feedback and yet performs quite well in turning maneuvers.

Cited Reference	Body Length [cm]	Weight [g]	Turning Radius [BL]	Turning Velocity [^{o}/s]
[38]	9.8	21.9	0.8	N/A
[4]	16.5	16.2	1.1	N/A
[39]	5.3	3	0.6	6
[40]	34	1100	0.47	36
[41]	56	3290	0.4	32.5
[42]	49.5	1290	0.3	200
[43]	40.5	1380	0.89	53
[44]	15	460	1	9
Robot (D)	37.5	1150	0.55	32
Robot (C)	37.5	1160	0.80	28.5
Robot (B)	36.5	1160	1.37	24
Robot (A)	36.5	1190	N/A	N/A

TABLE I

TURNING RADII (IN BODY LENGTHS, BL) AND TURNING VELOCITY OF DIFFERENT ROBOTS.

VII. CONCLUSION AND FUTURE WORK

In this paper we investigated the effect of passive appendages on the locomotion of an aquatic robot. We presented and compared angular velocity data as well as position data of robots with differing passive tail morphologies. The motion of these robots was compared to the motion of a robot without a tail or any appendages. These robots are based on an experimental platform for aquatic robots that are entirely actuated by the motion of an internal momentum wheel. The experiments presented in this paper clearly demonstrate that the passive tails make the robots highly maneuverable. The improved maneuverability is a result of the fluid-tail structure interaction that modulates the location of vortex shedding and the sign of the circulation of the vorticity. Using a potential flow solver we computed the hydrodynamic moments imparted on different foil configurations and showed that when the foil possess a tail, the hydrodynamic moment exerted on the foil aids its turning motion for almost half the turning time period. The key factors that influence how much of the hydrodynamic moment is assisting the turning motion versus resisting the motion are the oscillation amplitude and the phase difference of the angular velocity of the tail with respect to that of the main body. The simulations in this paper support the experimental observation, that when the tail oscillates out of phase with the main body, the resistive hydrodynamic angular impulse experienced by the main body is reduced thus increasing the maneuverability of the foil.

Other factors can be expected to play a significant role in improving the passive maneuverability of natural swimmers. These factors include the geometry and placement of the passive appendages. For instance the passive appendages could be fin-like elements instead of tail-like elements. Another important factor is the stiffness of the passive appendages or joints, which can modify the phase difference between the tail and body angular velocity to improve the turning ability. We have not explored these factors in this paper, but only demonstrate the important fact that passive appendages with even zero stiffness could play a very significant role in improving the maneuverability with minimal sensing and feedback control.

The robots presented in this paper do not incorporate any feedback, are not streamlined or optimized for field trials, but are merely an experimental platform to test the fluid-tail structure interaction. Yet the maneuverability of the robots discussed in this paper is comparable to or even better than that of many swimming robots that utilize multiple actuators and sensors, and using feedback control algorithms. The findings in this paper suggest that passive dynamics inherent in the robot-fluid interaction can be exploited to control the motion of a swimming robot.

VIII. ACKNOWLEDGMENTS

This paper is based upon work supported by the National Science Foundation under grant number CMMI 1563315.

REFERENCES

[1] D.N. Beal, F.S. Hover, M.S. Triantafyllou, J.C. Liao, and G.V. Lauder. Passive propulsion in vortex wakes. *Journal of Fluid Mechanics*, 549:385–402, 2006.

[2] M. S. Triantafyllou and G. S. Triantafyllou. Propulsion through oscillating foils in nature and technology. *Journal of Fluids and Structures*, 7:205–224, 1993.

[3] H. Xiong. *Geometric Mechanics, Ideal Hydrodynamics, and the Locomotion of Planar Shape-Changing Aquatic Vehicles*. PhD thesis, University of Illinois at Urbana-Champaign, 2007.

[4] S. McGovern, G. Alici, Van-Tan Truong, and G. Spinks. Finding nemo (novel electromaterial muscle oscillator): a polypyrrole powered robotic fish with real-time wireless speed and directional control . *Smart Materials and Structures.*, 18(9):095009, 2009.

[5] B. P. Epps, K. Youcef-Toumi P. Valdivia Alvarado, and A. H. Techet. Swimming performance of a biomimetic compliant fish-like robot. *Experiments in Fluids*, 47:927–939, 2009.

[6] Z. Chen, S. Shatara, and X. Tan. Modeling of biomimetic robotic fish propelled by an ionic polymermetal composite caudal fin. *IEEE/ASME Transactions on Mechatronics*, 15(3):448–459, 2010.

[7] C. Rossi, J. Colorado, W. Coral, and A. Barrientos. Bending continuous structures with smas: a novel robotic fish design. *Bioinspiration and Biomimetics*, 6:045005, 2011.

[8] M. Rufo and M. Smithers. Ghostswimmer auv: Applying biomimetics to underwater robotics for achievement of tactical relevance. *Marine Technology Society Journal*, 45(4):24–30, 2011.

[9] V. Kopman and M. Porfiri. Design, modeling, and characterization of a miniature robotic fish for research and education in biomimetics and bioinspiration. *IEEE/ASME Transactions on Mechatronics*, 18(2):471–483, 2013.

[10] D. B. Quinn, G. V. Lauder, and A. J. Smits. Scaling the propulsive performance of heaving flexible panels. *Journal of Fluid Mechanics*, 7(38):250–267, 2014.

[11] S. Alben, C. Witt, T. V. Baker, E. Anderson, and G. V. Lauder. Dynamics of freely swimming flexible foils. *Physics of Fluids*, 24(5):051901, 2012.

[12] M. C. Leftwich, E. D. Tytell, A. H. Cohen, and A. J. Smits. Wake structures behind a swimming robotic lamprey with a passively flexible tail. *Journal of Experimental Biology*, pages 416–425, 2012.

[13] G. V. Lauder and P. G. A. Madden. Fish locomotion: kinematics and hydrodynamics of flexible foil-like fins. *Experiments in Fluids*, 43(5):641–653, 2007.

[14] H. Dong, R. Mittal, M. Bozkurttas, P. Madden, and G. Lauder. Computational modelling and analysis of the hydrodynamics of a highly deformable fish pectoral fin. *Journal of Fluid Mechanics*, 645:345–373, 2010.

[15] B. Flammang and G. Lauder. Caudal fin shape modulation and control during acceleration, braking and backing maneuvers in bluegill sunfish, lepomis macrochirus. *Journal of Experimental Biology,*, 212(2):277–289, 2009.

[16] M. Dickinson, F. Lehmann, and S. Sane. Wing rotation and the aerodynamic basis of insect flight. *Science*, 284(5422):1954–1960, 1999.

[17] R. Pfeifer, M. Lungarella, and F. Iida. Self-organization, embodiment, and biologically inspired robotics. *science*, 318(5853):1088–1093, 2007.

[18] A. J. Bergou, L. Ristroph, J. Guckenheimer, I. Cohen, and Z. J. Wang. Fruit flies modulate passive wing pitching to generate in-flight turns. *Physical review letters*, 104(14):148101, 2010.

[19] P.W. Webb and A.J. Cotel. Turbulence: does vorticity affect the structure and shape of body and fin propulsors? *Integrative and comparative biology*, page icq020, 2010.

[20] F.E. Fish and G.V. Lauder. Passive and active flow control by swimming fishes and mammals. *Annu. Rev. Fluid Mech.*, 38:193–224, 2006.

[21] A. H. Techet, F.S. Hover, and M. S. Triantafyllou. Separation and turbulence control in biomimetic flows. *Flow, Turbulence and Combustion*, 71(1-4):105, 2003.

[22] M.S. Triantafyllou, A.H. Techet, Q Zhu, D.N. Beal, F.S Hover, and D.K.P. Yue. Vorticity control in fish-like propulsion and maneuvering. *Integrative and comparative biology*, 42(5):1026–1031, 2002.

[23] Q. Bone. Muscular and energetic aspects of fish swimming. In *Swimming and flying in nature*, pages 493–528. Springer, 1975.

[24] B. C. Jayne, A. F. Lozada, and G. V. Lauder. Function of the dorsal fin in bluegill sunfish: motor patterns during four distinct locomotor behaviors. *Journal of Morphology*, 228(3):307–326, 1996.

[25] B. Pollard and P. Tallapragada. An aquatic robot propelled by an internal rotor. *IEEE/ASME Transaction on Mechatronics*, 22(2):931–939, 2017.

[26] M H. Dickinson, C. T. Farley, R. J. Full, M. Koehl, R. Kram, and S. Lehman. How animals move: an integrative view. *Science*, 288(5463):100–106, 2000.

[27] J. G. Cham, J. K. Karpick, and M. R. Cutkosky. Stride period adaptation of a biomimetic running hexapod. *The International Journal of Robotics Research*, 23(2):141–153, 2004.

[28] P. Tallapragada and S. D. Kelly. Reduced-order modeling of propulsive vortex shedding from a free pitching hydrofoil with an internal rotor. In *Proceedings of the 2013 American Control Conference*, 2013.

[29] P. Tallapragada and S. D. Kelly. Dynamics and self-propulsion of a spherical body shedding coaxial vortex rings in an ideal fluid. *Regular and Chaotic Dynamics*, 18:21–32, 2013.

[30] P. Tallapragada and S. D. Kelly. Self-propulsion of free solid bodies with internal rotors via localized singular vortex shedding in planar ideal fluids. *The European Physical Journal Special Topics*, 2015.

[31] P. Tallapragada. A swimming robot with an internal rotor as a nonholonomic system. *Proceedings of the American Control Conference, 2015*, 2015.

[32] Stephen Childress. *Mechanics of swimming and flying*. Cambridge University Press, 1981.

[33] K. Streitlien, G. S. Triantafyllou, and M. S. Triantafyllou. Efficient Foil Propulsion Through Vortex Control. *AIAA Journal*, 34:2315–2319, 1996.

[34] M. S. Triantafyllou, G. S. Triantafyllou, and D. K. P. Yue. Hydrodynamics of fishlike swimming. *Annual Reviews of Fluid Mechanics*, 32:33–53, 2000.

[35] J. L. Hess and A. Smith. Calculation of potential flow about arbitrary bodies. *Progress in Aerospace Sciences*, 8:1–138, 1967.

[36] J. Katz and A. Plotkin. *Low-Speed Aerodynamics*. Cambridge University Press, 2001.

[37] J. Melli. *A Hierarchy of Models for the control of Fish-like Locomotion*. PhD thesis, Princeton University, 2008.

[38] X. Ye, Y. Su, and S. Guo. A centimeter-scale autonomous robotic fish actuated by ipmc actuator. In *Robotics and Biomimetics, 2007. ROBIO 2007. IEEE International Conference on*, pages 262–267. IEEE, 2007.

[39] X. Ye, Y. Su, S. Guo, and T. Wang. Infrared motion guidance and obstacle avoidance of an icpf actuated underwater microrobot. In *Mechatronics and Automation, 2007. ICMA 2007. International Conference on*, pages 1851–1856. IEEE, 2007.

[40] K. Hirata, T. Takimoto, and K. Tamura. Study on turning performance of a fish robot. In *First International Symposium on Aqua Bio-Mechanisms*, pages 287–292, 2000.

[41] J. Yu, Z. Su, M. Wang, M. Tan, and J. Zhang. Control of yaw and pitch maneuvers of a multilink dolphin robot. *IEEE Transactions on robotics*, 28(2):318–329, 2012.

[42] Z. Su, J. Yu, M. Tan, and J. Zhang. Implementing flexible and fast turning maneuvers of a multijoint robotic fish. *IEEE/ASME Transactions on Mechatronics*, 19(1):329–338, 2014.

[43] J. Yu, L. Liu, L. Wang, M. Tan, and D. Xu. Turning control of a multilink biomimetic robotic fish. *IEEE Transactions on Robotics*, 24(1):201–206, 2008.

[44] S. B. Behbahani, J. Wang, and X. Tan. A dynamic model for robotic fish with flexible pectoral fins. In *IEEE/ASME International Conference on Advanced Intelligent Mechatronics (AIM)*, pages 1552 –1557, 2013.

AUTHOR BIOGRAPHIES

Beau Pollard received the B.S degree in Mechanical Engineering from Clemson University in 2015. He is currently working towards the Ph.D degree in Mechanical Engineering at the department of Mechanical Engineering in Clemson University. His current research interests include nonlinear dynamics, bio inspired swimming robots and fluid-structure interaction.

Phanindra Tallapragada received the B.Tech and M.Tech degrees from the Indian Institute of Technology, Kharagpur in 2004. He received an M.S. in Mathematics and Ph.D in Engineering Mechanics from Virginia Tech in 2010. He was a postdoctoral fellow at UNC Charlotte between 2010 and 2013. He has been an assistant professor in the department of Mechanical Engineering at Clemson University since August 2013. His current research interests include nonlinear dynamics, geometric mechanics, nonholonomic mechanical systems, vortex dynamics, bio inspired swimming robots and locomotion in low Reynolds number flows.